We are IntechOpen,
the world's leading publisher of
Open Access books
Built by scientists, for scientists

6,900
Open access books available

186,000
International authors and editors

200M
Downloads

Our authors are among the

154
Countries delivered to

TOP 1%
most cited scientists

12.2%
Contributors from top 500 universities

Interested in publishing with us?
Contact book.department@intechopen.com

Numbers displayed above are based on latest data collected.
For more information visit www.intechopen.com

Interferometry for Fusion Devices

Luis Esteban and Miguel Sánchez
CIEMAT-EURATOM Association
Spain

1. Introduction

Interferometers are optical arrangements capable of measuring changes in the optical paths by measuring the phase differences. They allow to perform a wide range of measurements, including the measurement of the line-electron density of the fusion plasmas Innocente & Tudisco (2006); Innocente et al. (1997); Joffrin & Riva (2003); Kornejew et al. (2006); Sanchez et al. (2008); Zeeland et al. (2006):

$$\int_0^{L_p} n_e \mathrm{d}l, \tag{1}$$

where n_e is the electron density and L_p is the integration path in the plasma.

The interferometric measurements are obtained through the observation of the interference between two or more beams, generally obtained by splitting an incident beam.

The solution to the electromagnetic free space wave equation can be expressed as:

$$\mathbf{E}(\mathbf{r}, t) = \mathbf{E}(\mathbf{r}) e^{i(\mathbf{k}\cdot\mathbf{r} - \omega t + \phi)}, \tag{2}$$

$\mathbf{E}(\mathbf{r})$ is the amplitude vector, ω is the angular frequency, and $\mathbf{k}$ is the wave number vector:

$$k = \frac{2\pi}{\lambda} \cdot \mathbf{e}_k, \tag{3}$$

where λ is the wavelength in the medium, and $\mathbf{e}_k$ is a unitary vector in the direction of the propagation.

In general, interferometers use at least two beams, probing and reference, following different optical paths, L_1 and L_2, which finally interfere in an square law detector[1]. The optical paths are given by:

$$L = \int_{path(t)} N \mathrm{d}l, \tag{4}$$

where the integration is taken along a geometric path with a fixed origin (beam splitter) and end (detector), N is the refractive index.

Considering that these waves have angular frequencies ω_1 and ω_2, and that they are plane, monochromatic, and coherent (from the same source), in this case the following approximation to the electric fields is considered:

$$u_1 = u_{01} e^{i(k_{01} \cdot L_1(t) - \omega_1 t + \phi_{01})}, \tag{5}$$

---

[1] An square law detector measures intensities

$$u_2 = u_{02}e^{i(k_{02}\cdot L_2(t) - \omega_2 t + \theta_{02})}. \tag{6}$$

At the detector, the interference signal has the form:

$$I = (u_{01} + u_{02})^2 = I_1 + I_2 + 2\sqrt{I_1 I_2}\cos\left((\omega_1 - \omega_2)t + k_0 \cdot (L_1(t) - L_2(t))\right), \tag{7}$$

where I is the intensity modulated at frequency $\Omega = \omega_1 - \omega_2$, and I_1 and I_2 are the respective intensities of the two waves. Since $k_{01} \simeq k_{02}$, the average between the two values $k_0 = (k_{01} + k_{02})/2$, has been considered in Eq. 7. Using k_0, the effective wavelength can be expressed as:

$$\lambda_{eff} = \frac{2\lambda_1\lambda_2}{\lambda_1 + \lambda_2}. \tag{8}$$

The alternate current from the detector is:

$$i = i_0 \cos\left(\Omega t + \phi(t)\right), \tag{9}$$

the phase $\phi(t)$ corresponds to the optical path length differences.

Usually, both angular frequencies are equal (i.e., $\Omega = 0$), in this case, the interferometer is called homodyne. If $\Delta\omega \neq 0$ (the measuring and reference beams operate at slightly different frequencies), the interferometer is called heterodyne. The frequencies are typically shifted using Acousto-Optic-Modulators (AOM) for the infrared Ohtsuka & Sasaki (1974). However, other techniques can be adopted for this purpose, in agreement with the used wavelengths, for instance rotating gratings in the case of far-infrared wavelengths.

The phase $\phi(t)$ carries the information related to the difference in the optical path-lengths between the two beams, due to the mechanical movements or changes in the refractive index. The initial phases of the probing and the reference beams, θ_{01} and θ_{02}, are integration constants, which for convenience are considered zero.

With respect to the optical setup, two configurations that are commonly used for plasma refractive index measurements are the Michelson and the Mach-Zehnder schemes. However, in practice, the setups used in fusion are a mixture of these two optical configurations. Both are two-beam interferometers; in the case of the Michelson configuration, the incoming and outgoing beams, travel in the same direction and in opposite senses, while in the Mach-Zehnder one the propagation follows only one sense. The difference between both is shown in Figure 1.

This Chapter is structured as follows. In Section 2 the relation between the line-integrated electron density and the phase shift suffered by the waves that cross the plasma is deduced for a cold plasma model. In Subsection 2.2 extends the cold plasma model for weakly relativistic plasmas, such as those expected in the ITER tokamak. In Section 3 the possible wavelengths to be used in these type of diagnostics are discussed. Section 4 outlines the main characteristics of the middle IR interferometers at TJ-II and at W7-X. Finally the basic expressions of Gaussian beam propagation are developed in Section 6. In addition, several phase measuring algorithms are listed, and the interpolation phase measuring algorithm is described in detail. The main conclusions of the chapter are summarized in Section 8.
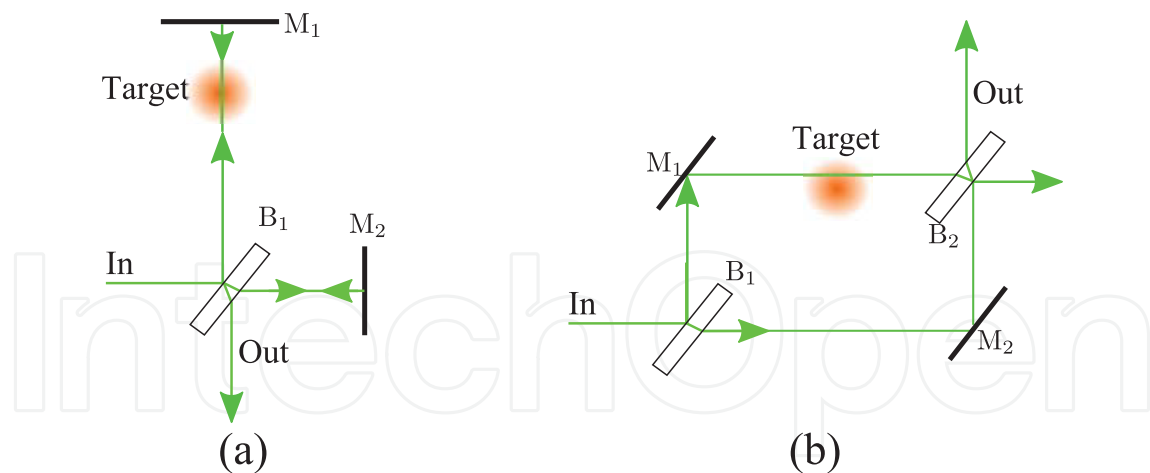
Fig. 1. a) A Michelson interferometer; the light is divided into two beams in the beam-splitter B_1; Both beams are reflected back at mirrors M_1 and M_2 and recombined in the output. b) A Mach-Zehnder interferometer. The incoming beam is divided in beam splitter B_1 into reference and measuring beams, which are reflected at mirrors M_1 and M_2, and finally recombined at beam splitter B_2.

2. Propagation of electromagnetic waves in plasmas

The expression to compute the line integrated electron density can be deduced from the Appleton-Hartree relation for a cold plasma. This expression would be valid for the TJ-II and the W7-X plasmas. However, for plasmas with an electron temperature of 20 eV, such as those expected at the ITER tokamak, a relativistic correction must be included in the line integrated electron density. In this Section the main expressions, for cold plasmas, Subsection 2.1 and for weakly relativistic plasmas, Subsection 2.2, are summarized. A detailed deduction can be found in Hartfuss et al. (1997); Hojo & Kawahata (2009); Hutchinson (1990).

2.1 Propagation of electromagnetic waves in cold plasmas

For the measurement of the electron density, the relation between this quantity and the changes in the refractive index of the plasma must be found.

Adopting the cold plasma approximation, the refractive index of the plasma is given by the Appleton-Hartree relation, Hartfuss et al. (1997); Hutchinson (1990):

$$N^2 = 1 - \frac{X(1-X)}{1 - X - \frac{1}{2}Y^2\sin^2\theta \pm \sqrt{\left[\left(\frac{1}{2}Y^2\sin^2\theta\right)^2 + (1-X)^2Y^2\cos^2\theta\right]}}. \tag{10}$$

If the magnetic field is negligible, $Y \to 0$, the refractive index becomes:

$$N^2 = 1 - X, \tag{11}$$

where:

$$X = \omega_p^2/\omega^2, \tag{12}$$

being ω_p the plasma frequency, and ω and the frequency of the radiation. The refractive index becomes:

$$N^2 = 1 - \frac{\omega_p^2}{\omega^2} = 1 - \frac{n_e}{n_c}, \tag{13}$$

n_e is the electron density and $n_{co} = \omega^2 m_e \epsilon_0 / e^2$ is the cutoff plasma density[2].

The phase shift suffered by an electromagnetic wave is given by Hutchinson (1990):

$$\phi = \int_{plasma} k(z)\mathrm{d}z. \tag{14}$$

In the particular case of interferometry, the measuring beam will travel through the plasma and also through vacuum. The vacuum contribution to the k vector can be removed comparing the phases of both measuring and reference beams Hartfuss et al. (1997); Hutchinson (1990):

$$\phi = \int_{plasma} (N(z) - 1)\frac{\omega}{c}\mathrm{d}z. \tag{15}$$

ω is the radiation frequency and c is the speed of light.

Substituting Eq. 13 in Eq. 15, the phase shift becomes:

$$\phi = \frac{\omega}{c} \int_{plasma} \left\{ \sqrt{\left(1 - \frac{n_e(z)}{n_c}\right)} - 1 \right\} \mathrm{d}z. \tag{16}$$

If $n_e \ll n_{co}$, the refractive index, N can be approximated by the first two terms of its Taylor expansion:

$$N \simeq 1 - \frac{1}{2}\frac{n_e}{n_c}, \tag{17}$$

the phase difference, ϕ becomes:

$$\phi = r_e \lambda \int_{plasma} n_e(z)\mathrm{d}z. \tag{18}$$

This integral receives the name o line integrated electron density, LID and for simplicity is denoted as $\int n_e(z)\mathrm{d}z$ Hartfuss et al. (1997). The LID measurement is computed after measuring the phase differences of the output signals, $\Delta\phi$ these phase differences are calculated around the carrying frequency Ω. The path across the plasma receives the name of chord length.

2.2 Corrections for weakly relativistic plasmas

In ITER, it is expected an electron temperature in the order of 20 keV, which implies that the cold plasma approximation is no longer valid. A correction factor β, must be included for the computation of the refractive index, Hojo & Kawahata (2009). Under these conditions, considering the dispersion relation for the ordinary mode, the refractive index would now become:

$$N = \sqrt{1 - \frac{1}{\beta}\frac{\omega_p^2}{\omega^2}}, \tag{19}$$

---

[2] The cutoff density establishes the minimum frequency of the waves that will propagate through the plasma. Below this value the propagation modes are evanescent

where a relativistic correction β, has been introduced:

$$\beta = \frac{3K_2(\rho)}{\rho^2 \int_0^\infty (p^4/\gamma^2)e^{-\rho\gamma}dp}, \tag{20}$$

$p = |\mathbf{p}|/(m_e c)$ is the normalized momentum, $\gamma = \sqrt{(1+p^2)}$, $\rho = m_e c^2/T_e$ and $K_2(\rho)$ is the modified Bessel function. Considering a weakly relativistic plasma ($\gamma < c$), $e^{-\rho\gamma}$ can be approximated by its Taylor expansion as:

$$e^{-\rho\gamma} \simeq e^{-\rho}e^{-\rho\frac{p^2}{2}}\left(1 + \rho\frac{p^4}{8}\right), \tag{21}$$

and the correction factor β can be simplified as Hojo & Kawahata (2009):

$$\beta \simeq 1 + \frac{5}{2\rho}, \tag{22}$$

if $n \ll n_{co}$ the phase difference can be finally written as:

$$\Delta\phi = \frac{\omega}{2cn}\frac{2\rho}{5+2\rho}\int_{z_1}^{z_2} n(z)dz. \tag{23}$$

3. Wavelength choice

In practice, these phase differences will not only occur due to plasma density variations, but also due to the mechanical vibrations and thermal drifts.

$$\phi = \phi_p + \frac{2\pi\Delta l}{\lambda}. \tag{24}$$

Mechanical vibrations, in one-color arrangements are one of the limiting factors for the wavelength choice. As it can be seen in the former equation, these effects become particularly important for low wavelengths. However, they can be suppressed using two-color setups. The upper limit is imposed by the cutoff density, n_{CO}, since when the probing wavelength is long enough it will not propagate through the plasma (evanescent modes). The probing wavelength must satisfy the next relation to ensure that it will propagate through the plasma:

$$\lambda < \frac{2\pi c}{e}\sqrt{\frac{m_e \epsilon_0}{n_{peak}}}, \tag{25}$$

where n_{peak} is the maximum electron plasma density and e and m_e are the electron charge and the electron mass respectively.

In interferometers operating in the middle infrared range, mechanical vibrations are higher than variations caused by plasma density fluctuations. This circumstance forces to use a second interferometer sharing the same optical path as the first one, so this contribution can be canceled in the final compensated signal[3]. These type of arrangements receive the name

---

[3] The compensated signal is obtained after subtracting the optical paths of both interferometers in order to cancel mechanical vibrations
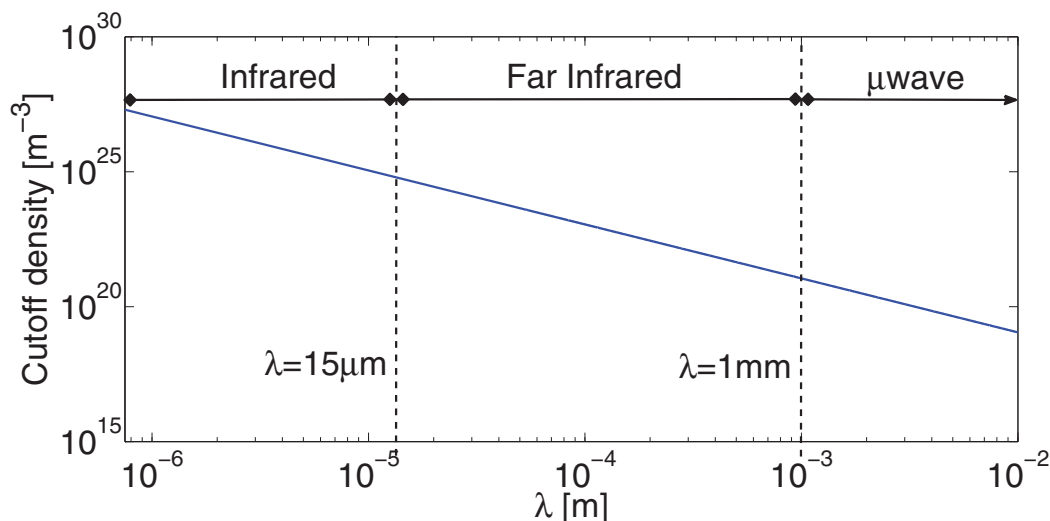
Fig. 2. Cutoff density versus wavelength from the middle infrared range to the μwave range. With shorter wavelengths higher densities can be measured. However, the vibration problem becomes more significant and forces to use two color arrangement.

of two-color interferometers. From Eq. 18 the optical path length difference from one of the interferometers is calculated as:

$$\lambda_1 \Delta\phi_1 = 2\pi r_e \lambda_1^2 \int_{\text{plasma}} n_e(l)\mathrm{d}l + \lambda_1 k_{01} \int_{\text{out}} N\mathrm{d}l, \tag{26}$$

The second term of the equation takes into account the optical path length outside the plasma. The final line integrated density is computed subtracting the optical path-length differences between both interferometers if the second term is canceled[4], Hartfuss et al. (1997); Hutchinson (1990):

$$\int n_e \mathrm{d}l = \frac{\Delta\phi_1 \lambda_1 - \Delta\phi_2 \lambda_2}{2\pi p \cdot r_e (\lambda_1^2 - \lambda_2^2)}, \tag{27}$$

p is an integer that corresponds to the number of times that the beams cross the plasma, r_e is the classical electron radius, λ_1 and λ_2 are the long and short wavelengths and $\Delta\phi_1$ and $\Delta\phi_2$ are the phase differences between the probing and reference signals of the two interferometers. Calculating the phase differences and hence the optical path length differences $\lambda_1 \Delta\phi_1$ and $\lambda_2 \Delta\phi_2$, the line integrated density is obtained from Eq. 27. An appropriate phase measuring algorithm is needed for this aim. Estimating the plasma chord-length (path-length for the line-integral), L_{chord}, the average density is evaluated as $< n_e >= \int n_e e \mathrm{d}l / L_{\text{chord}}$. The plasma chord-length depends on the plasma configuration, and is estimated using the spatial profile measured by the Thomson Scattering system, Herranz et al. (2008; 2000).

Another limiting factor, is that in practice plasmas are not uniform. A density gradient normally exists in the radial direction of the plasma, this will cause a deflection of the output beam with respect to the incident one, Figure 3. If the deflected angle, θ is large enough a miss alignment may occur and by the interference signal can be lost at the detector.

In general, the deflection angle is given by Hutchinson (1990):

$$\theta = \frac{\lambda}{2\pi} \frac{\mathrm{d}\phi}{\mathrm{d}y} = \frac{\mathrm{d}}{\mathrm{d}y} \int N\mathrm{d}l. \tag{28}$$

---

[4] The non-cancelation of the second term results in systematic error in the final electron density
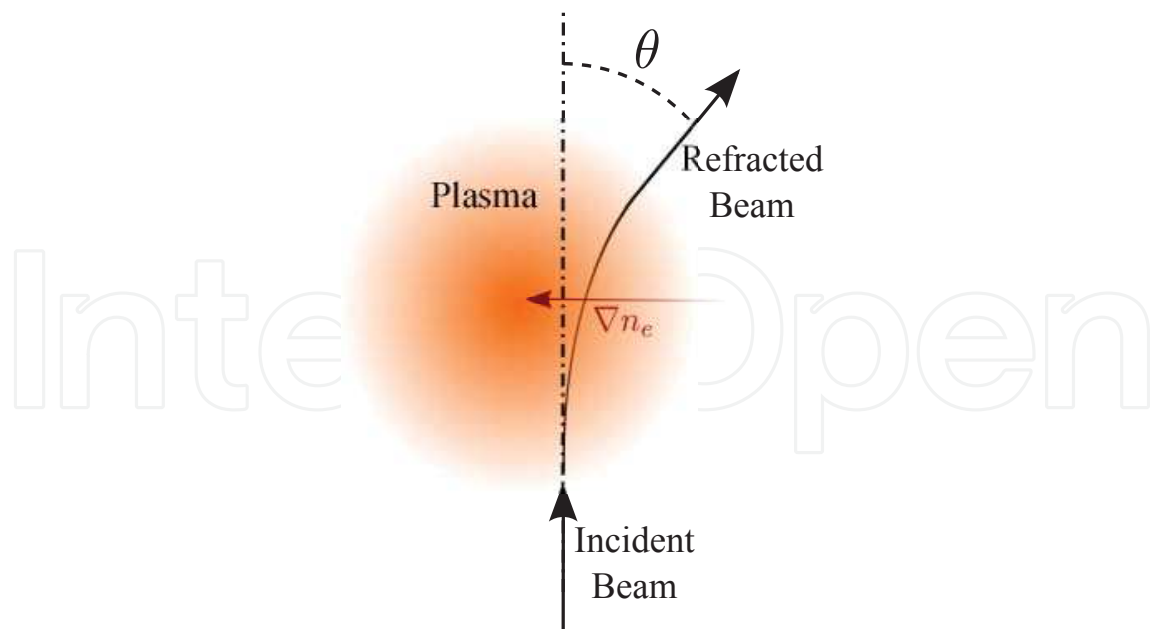
Fig. 3. Refraction suffered by a beam of light when crossing a non-uniform plasma.

Substituting Eq. 17 into the former equation, the deflection angle becomes:

$$\theta = \frac{\lambda^2 r_e}{2\pi} \int \nabla n_e \mathrm{d}l. \tag{29}$$

The deflection has a quadratic dependence with the wavelength, so for low wavelengths this effect is to be lower and for the range of interest in this chapter, $1.064 - 10.591$ μm, it is negligible. For example, if a parabolic density profile is considered, the maximum deflexion angle would be:

$$\theta = \frac{n_{peak} \lambda^2 e^2}{4\pi^2 c^2 \epsilon_0}, \tag{30}$$

where n_{peak} is the maximum electron density reached. Considering a peak density of 10^{20} m^{-3} the deflexion suffered by a 10.591 μm beam would be of 10^{-5} rad, which is several orders of magnitude below the typical alignment errors. However, for larger wavelengths, for instance in the far IR region this effect can be significant and should be taken into account. In Table **??** a summary of different wavelengths used in interferometers operating in TJ-II, W7-X, DIII-D, JET, LHD, Tore Supra and ITER fusion machines is shown Braithwaite et al. (1989); Brower et al. (2006); Gil et al. (2001); Kawahata et al. (1997); Kornejew et al. (2006); Zeeland et al. (2006).

4. Overview of the TJ-II and the W7-X interferometers

TJ II is a medium scale flexible Heliac type stellarator Alejaldre (2005) installed in the Laboratorio Nacional de Fusión of CIEMAT, Spain for the study of helical axis plasmas in a wide range of parameters Alejaldre (1989). TJ-II device has a major radius of 1.5 m, a minor of 0.28 m and the magnetic field generated in the center of the plasma is of 1 T. The plasma is heated using an ECRH[6] system based on two gyrotrons working at 53.2 GHz and delivering

---

[6] Electron Cyclotron Resonance Heating

Fusion Device	λ_1	λ_2	Peak density
TJ-II	$CO_2 - 10.6\ \mu m$	$NdYAG - 1.064\ \mu m$	$\sim 8 \cdot 10^{19}\ m^{-3}$
W7-X[5]	$CO_2 - 10.6\ \mu m$	$CO - 5.295\ \mu m$	$> 10^{20}\ m^{-3}$
DIII-D	$CO_2 - 10.6\ \mu m$	$HeNe - 0.633\ \mu m$	$> 10^{20}\ m^{-3}$
JET	$DCN - 195\ \mu m$	$CH_3OH - 118.8\ \mu m$	$> 10^{20}\ m^{-3}$
LHD	$CH_3OH - 118.8\ \mu m$	-	$> 10^{20}\ m^{-3}$
TORE SUPRA	$DCN - 195\ \mu m$	$CH_3OH - 118.8\ \mu m$	$> 10^{20}\ m^{-3}$
ITER	$CO_2 - 10.6\ \mu m$	$CO - 5.295\ \mu m$	$> 10^{22}\ m^{-3}$

Table 1. Optical configurations for interferometers operating in different fusion devices
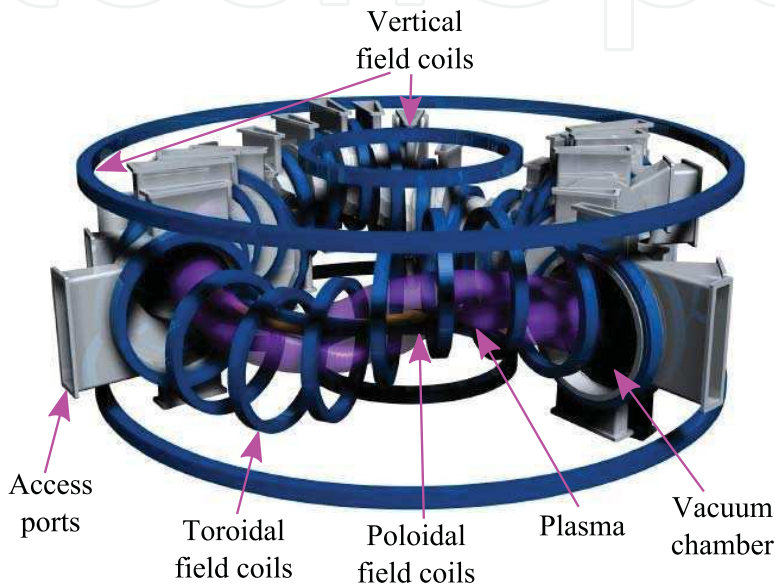

Fig. 4. Aerial and lateral view of the TJ-II device it has four periods, 32 toroidal coils, 2 poloidal coils and 2 vertical coils.

each up to 200 kW of power to the plasma, and NBI[7]. The maximum electronic densities reached are in the order of $8 \cdot 10^{19} m^{-3}$. To measure in this density range an heterodyne interferometer operating in the middle IR range is installed.

In IPP Greifswald the W7-X stellarator is currently in an advanced stage of construction. W7-X will be the biggest stellarator in the world. The major radius of W7-X will be of 5.5 m and the minor of 0.53 m with a maximum magnetic field in the axis of 3 T. W7-X will have ECRH heating systems in continuous mode (30 MW of power will be reached using this procedure), NBI and ICRH[8] (pulsed). W7-X device is an evolution of the W7-AS, being the first fusion device of the stellarator type with fully optimized, modular super-conducting coils aiming on high performance plasma under steady state conditions.

A key diagnostic that is being developed is a one channel two color heterodyne IR interferometer dedicated for density control and to control the Thomson scattering system Kornejew et al. (2006). It is planned to build it using CO_2 (10.591 μm) for the long wavelength and CO (5.295 μm) for the short one. The choice of the short wavelength has the purpose of

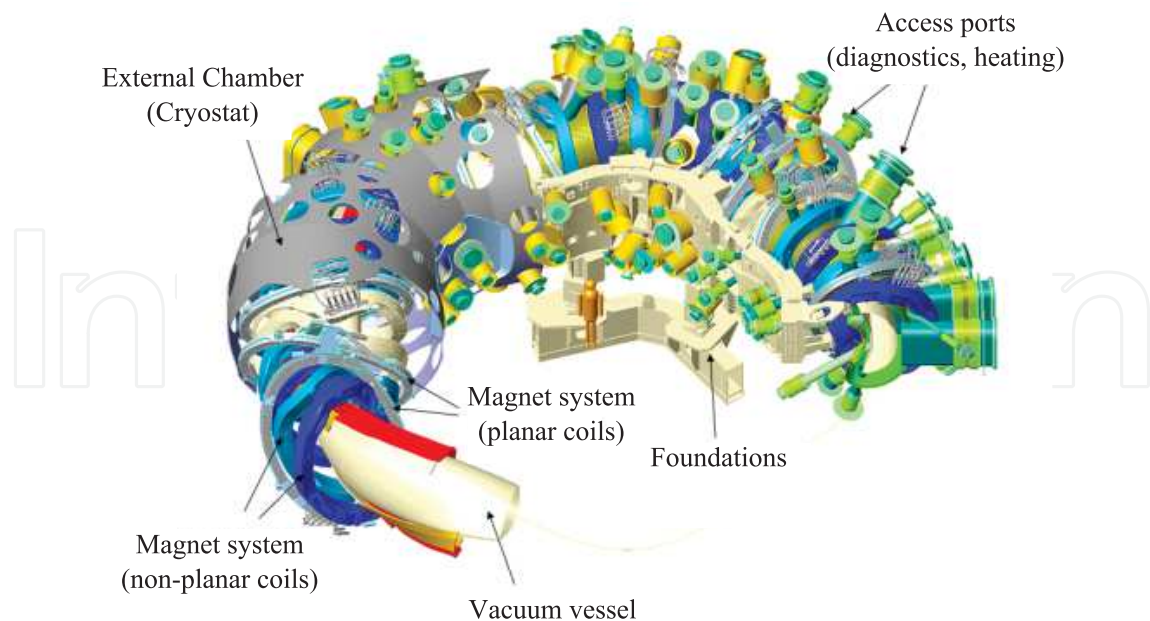[7] Neutral Beam Injection

[8] Ion Cyclotron Resonance Heating

Fig. 5. Detail of the W7-X Stellarator.

minimizing the thermo-optical effect in the vessel windows Sánchez & Sánchez (2005). The configuration CO_2-CO permits the use of one single detector for both wavelengths, however a correct frequency diplexion strategy must be fulfilled. There only exists one interferometer fusion diagnostic with a similar detection scheme Innocente & Tudisco (2006).

Both the IR interferometer at TJ-II and the test prototype currently installed at IPP-Greifswald use an hybrid Michelson Mach-Zhender configuration, with two colors to compensate mechanical vibrations and heterodyne modulation. For the shake of simplicity in Figure 6 a two color Mach-Zhender arrangement operating as a fusion diagnostic is illustrated. One arm of the interferometer crosses the plasma and the other arm that travels the same optical path is used as a reference. In the probing arm (the one that crosses the plasma) a frequency displacement ω_1 is introduced using Acousto-optical modulation. When the probing beam reaches an square law detector it interferes with the reference beam and an output signal is generated. The frequency of this signal is that of the displacement introduced, ω_1. The second interferometer is used to cancel mechanical vibrations and shares the same optical path as the first one. The final line-integrated density is obtained by subtracting the measures of both devices.

In the TJ-II infrared interferometer always important signal processing tasks have been carried out by traditional analog systems. The speed and accuracy needed for this application suggests to replace these type of systems by digital electronics. Taking into account the frequencies handled the only possible solution is the use of FPGAs. All the signal processing has been implemented in FPGA type devices.

5. Detection schemes at TJ-II and W7-X

In the TJ-II Stellarator the configuration CO_2 [10.591 μm] $-$ Nd : YAG [1.064 μm] forces to use two detectors, Figure 7. The two interference signals are sampled using two ADCs and the phases are compared with the phases of two reference signals extracted directly from the
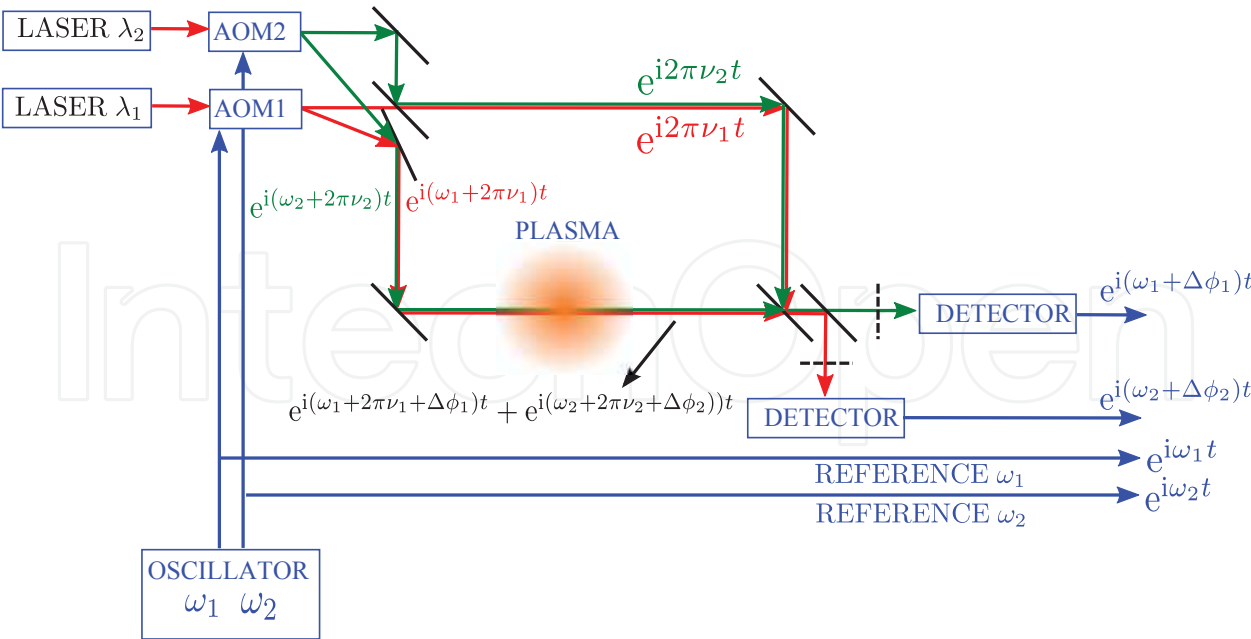
Fig. 6. Two color infrared heterodyne Mach-Zehnder interferometer employing a classical two detector scheme.
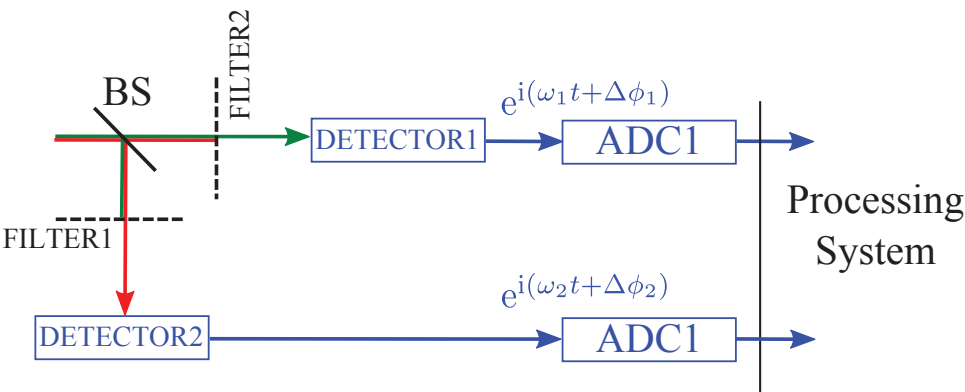

Fig. 7. Detection scheme based in two detectors, a beam splitter and two optical filters are needed to isolate the correspondent signals.

oscillator that drives the AOMs. In principle no electronic input split preprocessing filter is needed, however, in practice these are useful to increase the signal-to-noise ratio (SNR) of the input interference signals.

The combinations, CO_2 [10.591 μm] $-$ CO [5.295 μm] and CO_2 [12.1 μm] $-$ CO_2 [9 μm] are the ones planned to be used in the W7-X Stellarator and in the ITER Tokamak, respectively. In both cases the wavelengths can be detected by a single detector, Figure 8. Provided that the signals can be split using electronic filters the number of optical components can be significantly reduced. Taking into account the port restriction access in W7-X this would be a great advantage.

In the particular case of the W7-X interferometer, several detectors from Vigo system show the same response for both CO_2 [10.591 μm] and CO [5.295 μm] wavelengths. In Table **??** the
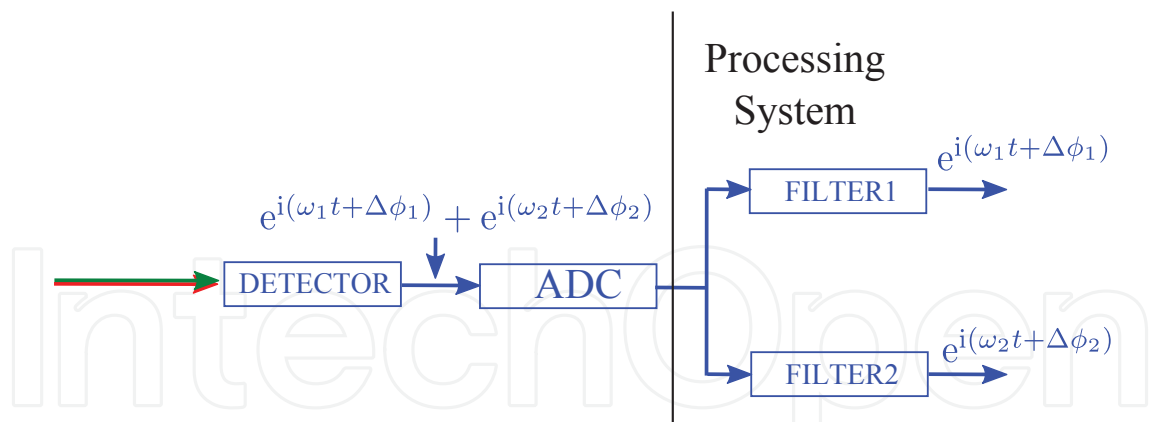
Fig. 8. Detection scheme based in two detectors, a beam splitter and two optical filters are needed to isolate the correspondent signals.

Detector	Detectivity at 5.296 [μm]	Detectivity at 10.591 [μm]
PVM-2TE-10.6	$0.8 \cdot 10^8$	$1.0 \cdot 10^8$
PCI-2TE-10.6	$2.0 \cdot 10^9$	$1.8 \cdot 10^9$
PVI-2TE-5	$5.0 \cdot 10^{11}$	$-$

Table 2. Detectivity for several Vigo Systems detectors at the wavelengths 5.296 μm and 10.591 μm. PV stands for photo-voltaic and PC for photo-conductive. The final choice has been the PCI-2TE-10.6.

detectivity[9] of these detectors is shown, being the photoconductive solution (PCI-2TE-10.6) the best.

The line-electron density measurement at W7-X will require a precision of 10^{18} m^{-2}, as it is described in Esteban, Sánchez, Sánchez, Kornejew, Hirsch, López, Fernández & Nieto-Taladriz (2010) the electronic filters needed to split both frequency components (CO$_2$ and CO interference signals), must have an attenuation in the rejection band of 43 dB. This task has been solved using digital filters Esteban, Sánchez, Sánchez, Kornejew, Hirsch, López, Fernández & Nieto-Taladriz (2010) implemented in hardware as a better alternative than the analog diplexer used in the Frascati Tokamak Innocente & Tudisco (2006). The intermediate modulating frequencies are of 25 MHz for the CO and of 40 MHz for the CO$_2$ and have been chosen in such a way that the useful bandwidth of the interferometer is not limited by the filters Kornejew et al. (2006); Sanchez et al. (2008).

6. Beam propagation

The predominant propagation modes of the lasers used are the TEM$_{00}$ the beams can be considered to be gaussian. The propagation of gaussian beams is well described in the classic literature Kogelnik & Li (1966); Self (1983), in this section the basic relations are summarized.

The beam intensity is given by:

$$I(r,z) = \frac{2}{\pi \omega^2} e^{-2\left(\frac{r}{\omega}\right)^2}. \tag{31}$$

---

[9] The detectivity is defined as the signal-to-noise ratio (SNR) at the detector output normalized to a 1 W radiant power, a 1 cm^2 detector optical area and a 1 HZ bandwidth
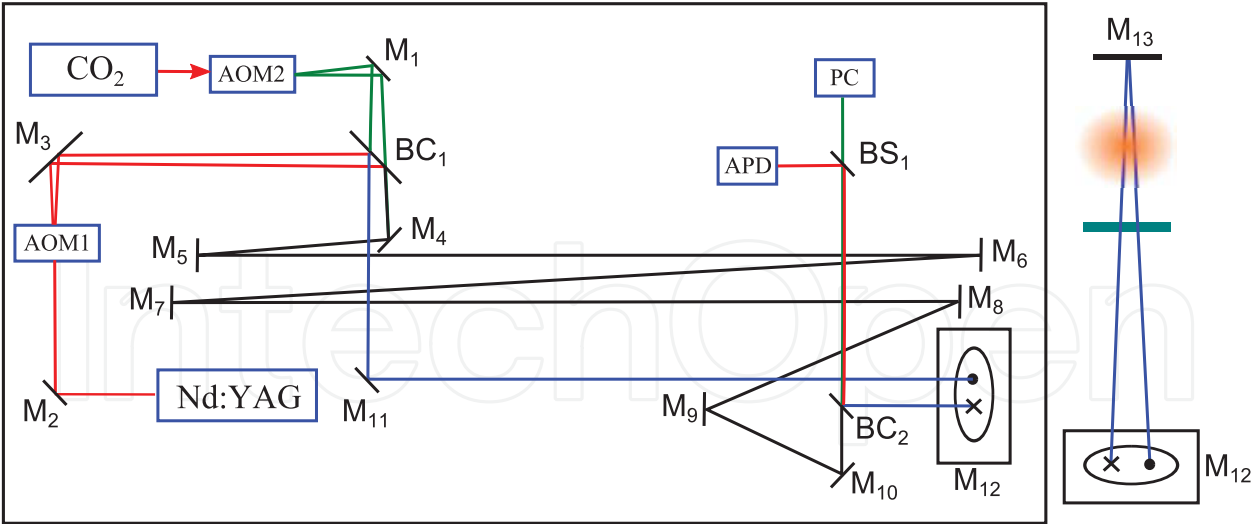
Fig. 9. Schematic layout of the one channel infrared interferometer of TJ-II, The green and red lines correspond to the CO_2 and Nd:YAG beams. The black line after the first beam combiner (BC_1) represents the path for both reference beams while the blue line represents the path for the probing beams. Both interference signals are detected in a photoconductor detector (PC), CO_2 and in an Avalanche Photo detector (APD), Nd:YAG. M_{12} is a periscope that launches both probing beams into the plasma, they cross a ZnSe window, the plasma and are reflected back to the periscope. The beam expander located at the output of the CO_2 sets both beam waists, Nd:YAG and CO_2 in the same position.

being, r the radius and ω the beam radius:

$$\omega(z) = \omega_0 \left[1 + \left(\frac{z}{z_R} \right)^2 \right], \qquad (32)$$

ω_0 is the beam waist and z_R is the Rayleigh range that separates the near and far fields:

$$z_R = \frac{\pi \omega_0^2}{\lambda}. \qquad (33)$$

The have angle beam divergence is given by:

$$\theta = M^2 \frac{\lambda}{\pi \omega_0}, \qquad (34)$$

where M^2 is the beam quality factor or the beam propagation factor.

In Figure 9 the schematic layout of the TJ-II infrared interferometer is illustrated and in In Figure **??** an unfolded virtual representation has been adopted for simplicity, in which the gaussian, Nd:YAG and CO_2 beams, travel in one direction and equal distances as they do in the interferometer, in this particular case 15 m until the beams reach the detectors.

Table **??** summarizes the main propagation characteristics of both lasers. At this point the Nd : YAG beam has a diameter of 5 cm and the CO_2 of 10 cm, the beam waists of both beams are located in the same positions so the curvature radius:

$$R(z) = z \left[1 + \left(\frac{z_R}{z} \right)^2 \right], \qquad (35)$$

Laser	Power [W]	θ [mrad]	ω_0 [mm]	M^2
Nd : YAG $-$ 1.064 μm	0.3	4	0.2	< 1.2
CO_2 $-$ 10.591 μm	8	5.5	1.5	< 1.2

Table 3. Propagation characteristics of the Nd:YAG and CO_2 beams, the curvature radius of both beams must be the same for equal axial positions. Both optical paths must share the same optical axis.

is the same at the detectors.

The power received by the detector is calculated integrating the radiation intensity, Eq. 31 over the detector area. If the detectors are located at a position z, such that the condition, $z \gg z_0$ is met, then the beam radius $\omega(z)$ can be approximated by:

$$\omega \simeq \omega_0 \frac{z}{z_R} = \frac{\lambda z}{\pi \omega_0}, \tag{36}$$

and the intensity, for one beam becomes:

$$I(r,z) = \frac{2\pi\omega_0}{\lambda^2 z^2} e^{-2\left(\frac{r\pi\omega_0}{\lambda z}\right)^2}. \tag{37}$$

Considering that both reference and probing beams reach the detector with intensities, I_1 and I_2 and knowing that the total interference intensity at one detector is:

$$I = I_1 + I_2 + 2\sqrt{I_1 I_2} \cos\left(2\pi\nu + \Delta\phi\right), \tag{38}$$

the AC component of the interference, $\sqrt{I_1 I_2}$ has been plotted together with the reference and probing intensities as it can be seen in Figure ?? the intensity of the interference is maximum when both probing and measuring intensities are equal, $I_1 = I_2$. This condition can be met by adjusting properly the AOMs.

As a final remark it should be notices that the beam waists of both colors must be located at the same geometrical positions this issue is specially important in multichannel interferometers. In this sense, three approaches can be considered to obtain the different chords:

1. Expanded beam,
2. Using independent modules,
3. Using beam splitters,

from the experience gain at TJ-II it can be said that the first is likely to be very sensitive to mechanical movements, in any case it should be ensures a high pointing stability of the beams.

7. Phase measurement

The line-electron density computation, indicated in Eq. 27 implies the use of an appropriate phase measuring algorithm. Several solutions have been developed in this sense. Some procedures are based on counting the cycles of a high speed clock in synchronism with the zero crossings of the probing signal (2004). These approaches, typically require a clock frequency higher than the frequency of the probing signals and are likely to suffer fringe jumps and synchronism problems if they are not carefully designed. Another method suitable for measuring phase shifts lower than one period of the input signal consist in decomposing
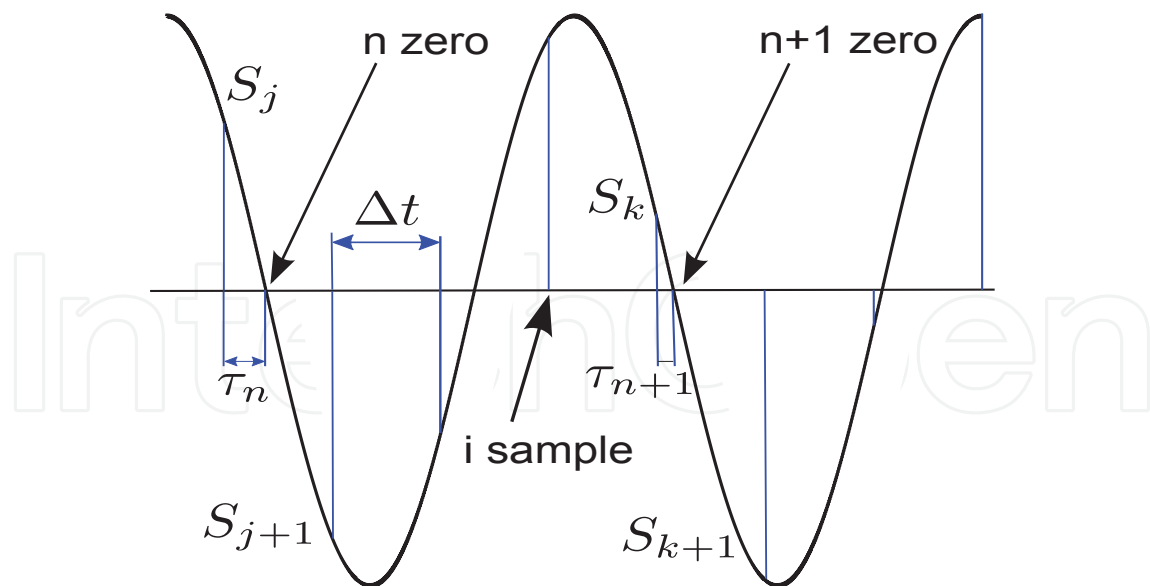
Fig. 10. Ilustration of the parameters involved in the interpolation algorithm. In this example just the negative edge zero crossings are considered.

the signals in its In-Phase & Quadrature components (IQ scheme). As the phase shifts in IR-interferometer operating as fusion diagnostic are of several periods the use of this technique requires of an additional fringe counting mechanism. Pulse width modulation based schemes are also used for phase measurements in interferometry Choi et al. (2005); Mlynek et al. (2010) Another method based on Analog-to-Digital conversion, ADC, zero crossing detection and linear interpolation Zubarev & Khilchenko (2003) was used in the TJ-II interferometer with good results Sanchez et al. (2004) this has been the deciding factor to implement this phase measuring algorithm in the real time measuring FPGA-based system. Below the IQ scheme and the interpolation algorithm are explained in detail.

7.1 Interpolation algorithm

During several TJ-II campaigns an interpolation algorithm has been used to compute the phase differences of the interferometric signals Sanchez et al. (2004). This algorithm counts both the zero crossings of the signals n, and the periods of time between zero crossings, Figure 10. Counting the number of samples in a period and adding it to the fraction of sample correspondent to each zero crossing, the phase at each sampling time can be obtained easily. The sample time fractions are computed interpolating linearly two consecutive samples around a zero cross, each value is given by Sanchez et al. (2004); Zubarev & Khilchenko (2003):

$$\tau_n = \frac{|S_j|}{|S_j| + |S_{j+1}|} \Delta t, \tag{39}$$

j is the number of zero crossings, Δt is the sample period and $|S_j|$ and $|S_{j+1}|$ are the absolute values of leading and trailing samples of a zero crossing. The total time elapsed at the j zero crossing is given by:

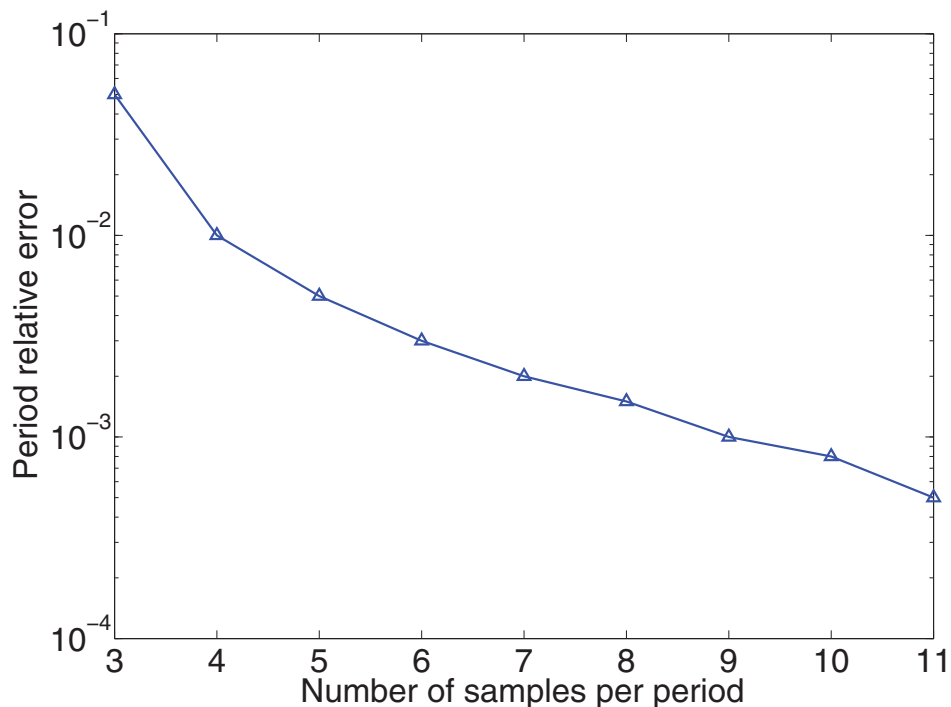$$t_n = j\Delta t + \tau_n. \tag{40}$$

Fig. 11. Interpolation error according to the number of samples per period of the signals, as it can be seen in the figure with less than four samples per period the error increases abruptly.

Using the same procedure, t_{n+1} can be calculated. The calculation of the phase value correspondent at sample time i is:

$$\varphi_i = 2\pi n + \frac{2\pi[(i-j)\Delta t - \tau_n]}{t_{n+1} - t_n}. \tag{41}$$

Where $t_{n+1} - t_n$ is the current period. in Figure 11 the error introduced by the algorithm for different numbers of samples per period is illustrated

Precisions of $1/400$ of CO_2 fringe have been achieved with this algorithm . This precision is equivalent to an error in the line integrated density of $\pm 10^{17} \text{m}^{-3}$. The algorithm was implemented in an off-line processing system and has been routinely working since autumn of 2003. Currently the FPGA-based processing is installed in the TJ-II IR-interferometer, allowing the readout of control signals and the processing of the electron density signal in real time Esteban et al. (2011); Esteban, Sánchez, López, Nieto-Taladriz & Sánchez (2010).

8. Conclusions

Several factors affect the propagation of electromagnetic waves in the plasmas and they affect the phase shift suffered by these waves. In most cases, the cold plasma approximation is valid. However, for electron temperatures in the order of tens of keV, relativistic effects become important, and a correction factor must be included in the equation that relates the phase shifts with the line integrated electron density.

The cutoff plasma frequency, mechanical vibrations and refraction are limiting parameters for the probing wavelengths. For high plasma densities, these limiting factors force

to use short wavelengths, that are specially sensitive to mechanical vibrations. These mechanical vibrations are canceled using another interferometer with a shorter wavelength, and subtracting both results.

The optical setup of both, the two-color one-channel interferometer at the TJ-II and the two color interferometer planned to be installed at the W7-X, have been described. They both operate in the middle infrared range to measure high density plasmas, and use heterodyne frequency displacement to cope with the phase sensitivity problem. In the particular case of the W7-X interferometer, the possibility of using a single detector is opened, which represents a challenge in the design of a frequency diplexor. The basic principles of gaussian beam propagation have been summarized, and illustrated for the TJ-II one-channel heterodyne interferometer. Also, an estimation of the signal-to-noise ratio at the output of both detectors has been calculated for the TJ-II interferometer. In addition several phase measuring algorithms for these type of interferometers have been listed, and the linear interpolation based algorithm used at the the TJ-II interferometer and tested at the W7-X one has been described.

9. References

(2004). *Measurement Science and Technology* 15: 2341–2348.

Alejaldre, C. (1989). Tj-ii project: A flexible heliac stellarator, *Fusion Technology* 17.

Alejaldre, C. (2005). Tj-ii the flexible heliac, *Europhysics News* pp. 232–233.

Braithwaite, G., Gottardi, N., Magyar, G., O'Rourke, J., Ryan, J. & Véron, D. (1989). Jet polari-interferometer, *Review of Scientific Instruments* 60(9): 2825–2834.
URL: *http://link.aip.org/link/?RSI/60/2825/1*

Brower, D. L., Deng, B. H. & Ding, W. X. (2006). Divertor interferometer diagnostic for iter, *Review of Scientific Instruments* 77(10): 10E911.
URL: *http://link.aip.org/link/?RSI/77/10E911/1*

Choi, H., Park, K. & La, J. (2005). Novel phase measurement technique of the heterodyne laser interferometer, *Review of Scientific Instruments* 76(9): 093105.
URL: *http://link.aip.org/link/?RSI/76/093105/1*

Esteban, L., Sánchez, M., López, J. A., Nieto-Taladriz, O., Kornejew, P. & Hirsch, M. (2011). Development of efficient fpga-based multi-channel phase meters for ir-interferometers, *IEEE Transactions on Nuclear Science* 58: 1562 – 1569.

Esteban, L., Sánchez, M., López, J. A., Nieto-Taladriz, O. & Sánchez, J. (2010). Continuous plasma density measurement in tj-ii infrared interferometer-advanced signal processing based on fpgas, *Fusion Engineering and Design* .

Esteban, L., Sánchez, M., Sánchez, J., Kornejew, P., Hirsch, M., López, J. A., Fernández, A. & Nieto-Taladriz, O. (2010). Continous phase measurement in the w7-x ir-interferometer by means of an fpga and high speed adcs, *Fusion Science and Technology* .

Gil, C., Elbeze, D. & Portafaix, C. (2001). Development of the ir interfero-polarimeter for long pulse operation at tore supra, *Fusion Engineering and Design* 56-57: 969 – 973.
URL: *http://www.sciencedirect.com/science/article/B6V3C-44JDTMG-5G/2/6ec2412225de2 81427fb48803f2d8b58*

Hartfuss, H. J., Geist, T. & Hirsch, M. (1997). Heterodyne methods in millimetre wave plasma diagnostics with applications to ece, interferometry and reflectometry, *Plasma Physics*

and Controlled Fusion 39(11): 1693.
URL: *http://stacks.iop.org/0741-3335/39/i=11/a=001*

Herranz, J., Castejón, F. & Pastor, I. (2008). Herranz, castejón, and pastor reply:, *Phys. Rev. Lett.* 101(13): 139504.

Herranz, J., Pastor, I., Castejón, F., de la Luna, E., García-Cortés, I., Barth, C. J., Ascasíbar, E., Sánchez, J. & Tribaldos, V. (2000). Profile structures of tj-ii stellarator plasmas, *Phys. Rev. Lett.* 85(22): 4715–4718.

Hojo, H. & Kawahata, K. (2009). Interferometry for weakly relativistic plasmas, *Plasma and Fusion Research* 4: 010.

Hutchinson, I. H. (1990). *Principles of plasma diagnostics*, Cambridge University Press.

Innocente, A. C. P. & Tudisco, O. (2006). Two-color medium-infrared scanning interferometer for the frascati tokamak upgrade fusion test device, *Applied Optics* 45(36): 9105–9114.

Innocente, P., Martini, S., Canton, A. & Tasinato, L. (1997). Upgrade of the rfx co[sub 2] interferometer using in-vessel optics for extended edge resolution, *Review of Scientific Instruments* 68(1): 694–697.
URL: *http://link.aip.org/link/?RSI/68/694/1*

Joffrin, P. I. D. M. E. & Riva, M. (2003). Real-time fringe correction algorithm for the jet interferometer, *Rev. Sci. Instrum.* 74: 3645–3653.

Kawahata, K., Ejiri, A., Tanaka, K., Ito, Y. & Okajima, S. (1997). Design and construction of a far infrared laser interferometer for the lhd, *Fusion Engineering and Design* 34-35: 393 – 397. Fusion Plasma Diagnostics.
URL: *http://www.sciencedirect.com/science/article/B6V3C-3SN5TJ5-2H/2/2f9f024cce400 6745e3f824b0609ad87*

Kogelnik, H. & Li, T. (1966). Laser beams and resonators, *Appl. Opt.* 5(10): 1550–1567.
URL: *http://ao.osa.org/abstract.cfm?URI=ao-5-10-1550*

Kornejew, P., Hirsch, M., Bindemann, T., Dreier, A. D. H. & Hartfuss, H. J. (2006). Design of multichannel laser interferometry for w7-x, *Rev. Sci. Instrum.* 77: 10F128.

Mlynek, A., Schramm, G., Eixenberger, H., Sips, G., McCormick, K., Zilker, M., Behler, K., Eheberg, J. & Team, A. U. (2010). Design of a digital multiradian phase detector and its application in fusion plasma interferometry, *Review of Scientific Instruments* 81(3): 033507.
URL: *http://link.aip.org/link/?RSI/81/033507/1*

Ohtsuka, Y. & Sasaki, I. (1974). Laser heterodyne measurement of small arbitrary displacements, *Optics Comunications* 10(4): 362–365.

Sanchez, M., Esteban, L., Kornejew, P. & Hirsch, M. (2008). Admissible crosstalk limits in a two colour interferometer for plasma density diagnostics. a reduction algorithm., *AIP Conference Proceedings* 993(1): 187–190.
URL: *http://link.aip.org/link/?APC/993/187/1*

Sanchez, M., Sanchez, J., Estrada, T., Sanchez, E., Acedo, P. & Lamela, H. (2004). High resolution co[sub 2] interferometry on the tj-ii stellarator by using an adc-based phase meter, *Review of Scientific Instruments* 75(10): 3414–3416.
URL: *http://link.aip.org/link/?RSI/75/3414/1*

Self, S. A. (1983). Focusing of spherical gaussian beams, *Applied Optics* 22(5): 658–661.

Sánchez, M. & Sánchez, J. (2005). Thermo-optical effect in zinc selenide windows for two-color interferometer for fusion plasma diagnostics, *Rev. Sci. Instrum.* 76: 046104–046104.

Zeeland, M. A. V., Boivin, R. L., Carlstrom, T. N., Deterly, T. & Finkenthal, D. K. (2006). Fiber optic two-color vibration compensated interferometer for plasma density

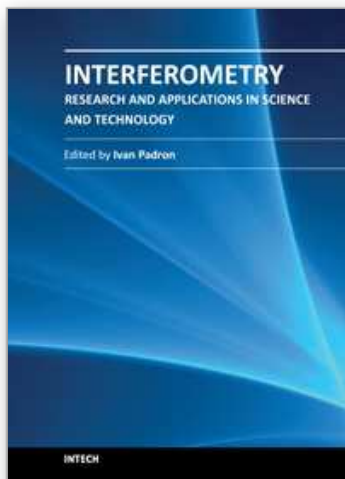measurements, *Review of Scientific Instruments* 77(10): 10F325.
        URL: *http://link.aip.org/link/?RSI/77/10F325/1*
Zubarev, P. V. & Khilchenko, A. D. (2003). Precision phase discriminator for the heterodyne
        interferometric plasma-density measurement technique, *Instruments and Experimental
        Techniques* 46: 171–176. 10.1023/A:1023661531511.
        URL: *http://dx.doi.org/10.1023/A:1023661531511*

Interferometry - Research and Applications in Science and Technology
Edited by Dr Ivan Padron

ISBN 978-953-51-0403-2
Hard cover, 462 pages
Publisher InTech
Published online 21, March, 2012
Published in print edition March, 2012

This book provides the most recent studies on interferometry and its applications in science and technology. It is an outline of theoretical and experimental aspects of interferometry and their applications. The book is divided in two sections. The first one is an overview of different interferometry techniques and their general applications, while the second section is devoted to more specific interferometry applications comprising from interferometry for magnetic fusion plasmas to interferometry in wireless networks. The book is an excellent reference of current interferometry applications in science and technology. It offers the opportunity to increase our knowledge about interferometry and encourage researchers in development of new applications.

How to reference
In order to correctly reference this scholarly work, feel free to copy and paste the following:

Luis Esteban and Miguel Sánchez (2012). Interferometry for Fusion Devices, Interferometry - Research and Applications in Science and Technology, Dr Ivan Padron (Ed.), ISBN: 978-953-51-0403-2, InTech, Available from: http://www.intechopen.com/books/interferometry-research-and-applications-in-science-and-technology/interferometry-for-magnetic-fusion-plasmas

INTECH
open science | open minds